Research Article

# Self-supported NiFe-LDH nanosheets on NiMo-based nanorods as high-performance bifunctional electrocatalysts for overall water splitting at industrial-level current densities

Yan Zhang[1], Biao Feng[1], MingLei Yan[2], Zhen Shen[1], Yiqun Chen[1], Jingyi Tian[1], Fengfei Xu[1], Guanghai Chen[1], Xizhang Wang[1], Lijun Yang[1], Qiang Wu[1] (✉), and Zheng Hu[1] (✉)

[1] Key Laboratory of Mesoscopic Chemistry of Ministry of Education (MOE) and Jiangsu Provincial Lab for Nanotechnology, School of Chemistry and Chemical Engineering, Nanjing University, Nanjing 210023, China
[2] College of Water Conservancy and Hydropower Engineering, Sichuan Agricultural University, Ya'an 625014, China

## ABSTRACT

Efficient, durable and economic electrocatalysts are crucial for commercializing water electrolysis technology. Herein, we report an advanced bifunctional electrocatalyst for alkaline water splitting by growing NiFe-layered double hydroxide (NiFe-LDH) nanosheet arrays on the conductive NiMo-based nanorods deposited on Ni foam to form a three-dimensional (3D) architecture, which exhibits exceptional performances for both hydrogen evolution reaction (HER) and oxygen evolution reaction (OER). In overall water splitting, only the low operation voltages of 1.45/1.61 V are required to reach the current density of 10/500 mA·cm$^{-2}$, and the continuous water splitting at an industrial-level current density of 500 mA·cm$^{-2}$ shows a negligible degradation (1.8%) of the cell voltage over 1000 h. The outstanding performance is ascribed to the synergism of the HER-active NiMo-based nanorods and the OER-active NiFe-LDH nanosheet arrays of the hybridized 3D architecture. Specifically, the dense NiFe-LDH nanosheet arrays enhance the local pH on cathode by retarding OH$^-$ diffusion and enlarge the electrochemically active surface area on anode, while the conductive NiMo-based nanorods on Ni foam much decrease the charge-transfer resistances of both electrodes. This study provides an efficient strategy to explore advanced bifunctional electrocatalysts for overall water splitting by rationally hybridizing HER- and OER-active components.

## KEYWORDS

alkaline water splitting, bifunctional electrocatalysts, layered double hydroxides, high durability, industrial current densities

## 1   Instruction

Hydrogen (H$_2$) is a prospective green energy carrier to replace fossil fuels and achieve carbon neutralization. Electrocatalytic water splitting is one of the most sustainable hydrogen production methods due to high H$_2$ purity, high energy efficiency and zero carbon emission especially when combined with renewable wind and solar power [1–3]. In an electrolytic cell, the water splitting process is comprised of cathodic hydrogen evolution reaction (HER) and anodic oxygen evolution reaction (OER), which usually bear large overpotentials [3, 4]. To enhance the HER and OER, efficient electrocatalysts are needed to reduce the activation energy and boost the charge/mass transfer kinetics. To date, the most active electrocatalysts for HER and OER are precious Pt- and Ir/Ru-based materials, respectively [5–7]. The scarcity and high price of precious metals restrict their large-scale deployment [8, 9]. Among various water electrolysis technologies, the alkaline water splitting is attractive because of its advantage of employing earth-abundant nonprecious metal electrocatalysts to reduce the cost [10–14]. Recently, tremendous progress has been achieved in exploring cost-efficient HER and OER catalysts working in alkaline electrolytes [15–17]. However, most electrocatalysts could only operate optimally for either HER or OER under specific

electrolytic conditions. The nonnegligible mismatch between the optimal working environments for HER and OER catalysts is unfavorable to the overall efficiency of water electrolysis systems. In contrast, bifunctional electrocatalysts active to both HER and OER can improve overall water splitting (OWS) performance and simplify the electrolysis system, showing great convenience in practical applications [17–19]. Despite the great efforts and progresses on this issue so far, most of the reported bifunctional catalysts still exhibited the high cell voltage, limited current densities and poor stability (Tables S1 and S2 in the Electronic Supplementary Material (ESM)), which can't meet the requirements of industrial water splitting. Hence, developing efficient, durable and economic bifunctional catalysts for both HER and OER is imperative but highly challenging.

An intuitive and feasible strategy to develop bifunctional electrocatalysts for OWS is to hybridize two components with respective HER and OER activity together [9]. For HER, NiMo-based bimetallic catalysts have high conductivity and are highly active in alkaline conditions with the Ni atoms as active centers for water dissociation and Mo atoms responsible for hydrogen adsorption, leading to the reduced energy barrier [20–22]. For OER, transition metal-based layered double hydroxides (LDHs)

exhibit the most attractive performances in alkaline media but usually with low conductivity, leading to poor activity at high current density [23]. Experimental and theoretical studies revealed that nickel and iron are two favorable metals in transition metal-LDH to catalyze OER [23–25]. In addition, we notice that the porous metal foam as substrate favors rapid mass transport and high conductivity, beneficial to the high-current-density electrocatalysis for industrial application [26, 27]. In this study, we have constructed a bifunctional electrocatalyst for OWS by growing NiFe-LDH nanosheet arrays on the NiMo-based nanorods deposited on Ni foam (NF) to form a hybridized three-dimensional (3D) architecture, denoted as NiFe-LDH@NiMo-H$_2$@NF. The synergism of the HER-active NiMo-based nanorods and the OER-active NiFe-LDH nanosheet arrays of the hybridized 3D architecture leads to the self-enhanced local pH on cathode side, the enlarged electrochemically active surface area (ECSA) on anode side, as well as the ultra-small charge-transfer resistances of both electrodes. As a result, the NiFe-LDH@NiMo-H$_2$@NF hybrid exhibits extraordinary electrocatalytic performances for both HER (26 mV@10 mA·cm$^{-2}$; 74 mV@500 mA·cm$^{-2}$) and OER (172 mV@10 mA·cm$^{-2}$; 239 mV@500 mA·cm$^{-2}$). With NiFe-LDH@NiMo-H$_2$@NF bifunctional catalyst, the overall water electrolyzer achieves the low initial cell voltage of 1.61 V at an industrial-level current density of 500 mA·cm$^{-2}$ with an excellent durability of only 1.8% degradation after over 1000 h continuous test, demonstrating the great potential applications.

# 2 Experimental

## 2.1 Materials

Nickel(II) nitrate hexahydrate (Ni(NO$_3$)$_2$·6H$_2$O, analytical reagent (AR)), sodium molybdate dihydrate (Na$_2$MoO$_4$·2H$_2$O, AR), ferrous sulfate heptahydrate (FeSO$_4$·7H$_2$O, AR), potassium hydroxide (KOH, AR), hydrochloric acid (HCl, AR, 36.0%–38.0%), and ethanol (C$_2$H$_5$OH, AR) were purchased from Sinopharm Chemical Reagent Co., Ltd. Pt/C (20 wt.%), iridium oxide (IrO$_2$, 99.9%), ruthenium oxide (RuO$_2$, 99.9%), and Nafion 117 solution (5 wt.%) were purchased from Sigma-Aldrich. Ni foam (thickness: 1.7 mm) was purchased from Shanghai Tankii Alloy Material Co., Ltd.

## 2.2 Synthesis

### 2.2.1 Synthesis of NiMoO$_4$·xH$_2$O@NF

NiMoO$_4$·xH$_2$O nanorods (x is the quantity of crystal water) were grown on NF by a simple hydrothermal process. Ni(NO$_3$)$_2$·6H$_2$O (1 mmol) and Na$_2$MoO$_4$·2H$_2$O (1 mmol) were dissolved in 30 mL of ultra-pure water under continuous magnetic stirring for 20 min, and then the solution was transferred into a 50 mL Teflon-lined stainless-steel autoclave. A piece of pretreated NF (2 cm × 4 cm) was placed into the solution as substrate, which was etched in HCl solution (1 M) for about 15 min to remove the oxide layer on the surface, and washed with acetone, ultra-pure water and ethanol under ultrasonic condition in turn. Subsequently, the autoclave was heated at 160 °C for 6 h. The product was obtained by filtration, washing with deionized water and ethanol for several times, and drying at 60 °C for 10 h, denoted as NiMoO$_4$·xH$_2$O@NF. NiMoO$_4$·xH$_2$O powder was obtained from the same hydrothermal process without NF.

### 2.2.2 Synthesis of NiMo-H$_2$@NF

The NiMoO$_4$·xH$_2$O@NF was placed into a tubular furnace and heated to 450 °C with a heating rate of 3 °C·min$^{-1}$ under H$_2$/Ar atmosphere (10 vol.% H$_2$ + 90 vol.% Ar). After thermal reduction for 2 h, the resulting product was denoted as NiMo-H$_2$@NF. For

optimizing the reduction temperature, the NiMoO$_4$·xH$_2$O samples were thermally treated at different temperatures by the similar process, donated as NiMo-H$_2$-n@NF (n = 350, 400, 500, 550, and 600 °C). NiMo-H$_2$ powder was obtained from the same thermal reduction process with NiMoO$_4$·xH$_2$O powder.

### 2.2.3 Synthesis of NiFe-LDH@NiMo-H$_2$@NF, NiFe-LDH@NiMoO$_4$·xH$_2$O@NF, and NiFe-LDH@NF

The electrodeposition of NiFe-LDH was carried out in a three-electrode system, with the as-prepared NiMo-H$_2$@NF, a graphite rod, and an Ag/AgCl electrode as the working, counter, and reference electrodes, respectively, and 100 mL solution containing 0.015 mol Ni(NO$_3$)$_2$·6H$_2$O and 0.015 mol FeSO$_4$·7H$_2$O as electrolyte. The electrodeposition was carried out under the N$_2$ atmosphere at a constant potential of −1.0 V vs. Ag/AgCl for different time (30, 60, and 90 s). The obtained samples were labelled as NiFe-LDH-y@NiMo-H$_2$@NF (y = 30, 60, and 90). For comparison, NiFe-LDH was electrodeposited directly on the pretreated Ni foam and NiMoO$_4$·xH$_2$O@NF by the same method for 60 s, denoted as NiFe-LDH@NF and NiFe-LDH@NiMoO$_4$·xH$_2$O@NF. All samples were washed with ultra-pure water and ethanol, and vacuum-dried overnight. The mass loading of NiFe-LDH@NiMo-H$_2$ on Ni foam was ~ 4.0 mg·cm$^{-2}$. NiMoO$_4$·xH$_2$O, NiMo-H$_2$, and NiFe-LDH@NiMo-H$_2$ were obtained by ultrasonic treatment of corresponding materials on Ni foam for TEM test.

### 2.2.4 Synthesis of NiMo-H$_2$/NiFe-LDH@NF

20 mg NiMo-H$_2$ powder, 100 μL Nafion, and 900 μL ethanol were ultrasonicated for 120 min to obtain a homogeneous ink. Then, 0.4 mL of the ink was coated onto a piece of NiFe-LDH electrodeposited Ni foam (1 cm × 2 cm), followed by drying at 60 °C for 12 h in air. The mass loading of NiMo-H$_2$ and NiFe-LDH on Ni foam was controlled to be ~ 4.0 mg·cm$^{-2}$.

## 2.3 Characterizations

X-ray diffraction (XRD) patterns were recorded on a Panalytiacl: X'Pert Pro using a Cu Kα radiation at 40 kV and 40 mA. The micromorphology and structure were characterized by scanning electron microscopy (SEM, Hitachi, S-4800) at 5 kV and 10 μA, high-resolution transmission electron microscopy (HRTEM, JEM-2100), and high-angle annular dark-field scanning TEM (HAADF-STEM, Talos F200S G2) equipped with energy dispersive X-ray spectrometer (EDS, SUPER X) at 200 kV. The surface species were analyzed by X-ray photoelectron spectroscopy (XPS, VG ESCALAB MKII) with an Al X-ray source worked at 150 W.

## 2.4 Electrochemical measurements

The electrochemical measurements were conducted on Biologic VMP3 electrochemical workstation in a three-electrode setup, with Hg/HgO electrode (1 M KOH) and graphite rod (8 mm in diameter) as a reference and counter electrodes, and the catalysts on Ni foam (1 cm × 1 cm) as the working electrodes. The working electrodes were first activated by cyclic voltammetry (CV) at a scan rate of 50 mV·s$^{-1}$ for 30 cycles. The HER polarization curves were performed in N$_2$-saturated 1 M KOH solution by linear sweep voltammetry (LSV) with a sweep rate of 5 mV·s$^{-1}$. Similarly, the OER polarization curves were tested in N$_2$-saturated 1 M KOH solution by LSV at a scan rate of 5 mV·s$^{-1}$. To get ECSA, CV curves were performed at different scan rates (20–200 mV·s$^{-1}$) in the potential window of 0.2–0.3 V (vs. Hg/HgO). The electrochemical impedance spectroscopy (EIS) was measured at −0.1 V (vs. reversible hydrogen electrode (RHE)) for HER and 1.53 V (vs. RHE) for OER from 0.1 Hz to 100 kHz with an amplitude of 5 mV. The long-term durability was tested by

chronopotentiometry (CP) measurements at a constant current density. The OWS tests were conducted by a two-electrode setup, and the polarization curves were measured at a scan rate of 5 mV·s⁻¹. All the measured potentials versus Hg/HgO ($E_{Hg/HgO}$) electrode were converted to RHE ($E_{RHE}$) according to the equation of $E_{RHE} = E_{Hg/HgO} + 0.059$ pH + 0.098. All the polarization curves in this study were corrected by 95% $iR_s$ compensation ($i$ is current measured by LSV. $R_s$ is internal resistance), i.e., $E_{iR\text{-correction}} = E_{test} - 0.95iR_s$ ($E_{iR\text{-correction}}$ is the potential (vs. RHE) with $iR_s$ compensation. $E_{test}$ is the tested potential (vs. RHE) by electrochemical workstation). The $R_s$ was measured by EIS tests at 0 V vs. Hg/HgO.

# 3　Results and discussion

## 3.1　Synthesis and characterization of NiFe-LDH@NiMo-H₂@NF

The preparation and characterizations of NiFe-LDH@NiMo-H₂@NF are shown in **Fig. 1**. Specifically, NiMoO₄·xH₂O nanorods were firstly deposited on NF by a simple hydrothermal process (denoted as NiMoO₄·xH₂O@NF), and transformed into NiMo-H₂ nanorods by the subsequent thermal reduction in 10% H₂/Ar atmosphere at 450 °C for 2 h (denoted as NiMo-H₂@NF). Then, the NiFe-LDH nanosheets were grown on NiMo-H₂ nanorods array via electrodeposition to form the hybridized 3D architecture of NiFe-LDH@NiMo-H₂@NF catalyst (**Fig. 1(a)**). Similarly, the NiFe-LDH nanosheet arrays were grown on NiMoO₄·xH₂O@NF and pristine NF to obtain NiFe-LDH@NiMoO₄·xH₂O@NF and NiFe-LDH@NF for comparison (see experimental section and ESM for details).

SEM observations show that the NiMoO₄·xH₂O nanorods densely stand on the surface of NF, with the diameters of 100–200 nm and the length of dozens of micrometers, which transform to the mixed-phase NiMo-H₂ nanorods mainly consisting of Ni and MoO₂ with the same morphology and size (**Figs. 1(b)**, **1(c)**, and **1(g)**). The dense and ultrathin NiFe-LDH nanosheet arrays were then grown on the surface of NiMo-H₂ nanorods with the height of ∼ 150 nm through electrodeposition, leading to the hybridized 3D architecture of NiFe-LDH@NiMo-H₂@NF (**Figs. 1(d)** and **1(e)**). An obvious interface exists between NiMo-H₂ nanorods and NiFe-LDH nanosheets (**Figs. 1(e)** and **1(f)**). The lattice fringes with 0.201 and 0.340 nm interplanar distances in the nanorod region correspond to Ni (111) planes and MoO₂ (110) planes of NiMo-H₂. The lattice fringes with 0.269 and 0.258 nm interplanar distances in the nanosheet region correspond to the (101) and (021) planes of NiFe-LDH (**Fig. 1(f)** and **Fig. S1** in the ESM). These results are in agreement with the XRD characterizations (**Fig. 1(g)** and **Fig. S2** in the ESM). The numerous interconnected NiFe-LDH nanosheets form a porous network on NiMo-H₂ nanorods, which favors the gas release during water electrolysis (**Figs. 1(d)** and **1(e)**, and **Fig. S3** in the ESM) [28]. This strategy can effectively increase the density of NiFe-LDH nanosheets and the conductivity of the hybridized 3D architecture. In contrast, NiFe-LDH@NF shows porous nanosheet arrays with a much lower density and larger size of nanosheets than NiFe-LDH@NiMo-H₂@NF (**Fig. S4** in the ESM).
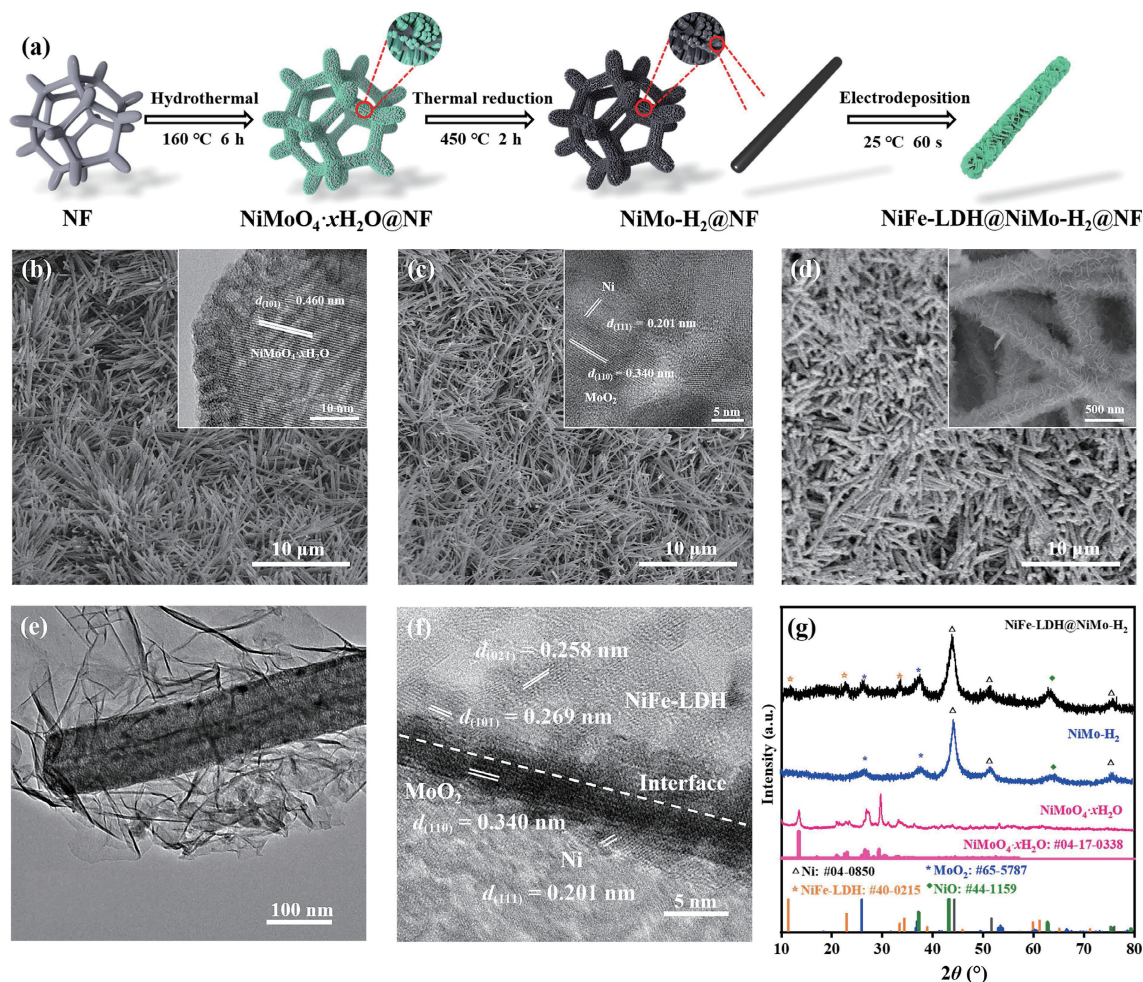


**Figure 1** Preparation and characterizations. (a) Schematic preparation route of NiFe-LDH@NiMo-H₂@NF. SEM images of (b) NiMoO₄·xH₂O nanorods, (c) NiMo-H₂ nanorods, and (d) NiFe-LDH@NiMo-H₂ grown on NF. Insets in ((b) and (c)) are corresponding HRTEM images and inset in (d) is local enlargement of SEM image. (e) TEM and (f) HRTEM images of NiFe-LDH@NiMo-H₂. (g) XRD patterns of the samples scratched from the NF.

The elemental valences of as-prepared materials were measured by XPS, as shown in Fig. 2. Ni, Mo, and O signals exist for NiMoO$_4$·$x$H$_2$O@NF and NiMo-H$_2$@NF. As expected, additional Fe signal appears for NiFe-LDH@NiMo-H$_2$@NF, and Ni, Fe, and O signals exist for NiFe-LDH@NF (Fig. 2(a)). For NiMoO$_4$·$x$H$_2$O@NF, the Ni species exist in Ni$^{2+}$ and Ni$^{3+}$ with the respective binding energy (BE) of 855.8/873.5 and 857.4/875.1 eV for 2p$_{3/2}$/2p$_{1/2}$, and the Mo species exists in Mo$^{6+}$ (BE = 232.2/235.4 eV for 3d$_{5/2}$/3d$_{3/2}$) [29]. After thermal reduction in H$_2$/Ar to NiMo-H$_2$@NF, the Ni species are reduced to Ni$^0$ (BE = 852.5/870.2 eV) and Ni$^{2+}$ (BE = 856.0/873.7 eV), and the Mo species are reduced to Mo$^{4+}$ (BE = 229.4/232.6 eV), trace Mo$^{5+}$ (BE = 230.3/233.5 eV), and residual Mo$^{6+}$ (BE = 232.2/235.4 eV) (Figs. 2(b) and 2(c)) [29–31]. The Mo$^{4+}$ species comes from the MoO$_2$ (Figs. 1(f) and 1(g)). In contrast, for NiFe-LDH@NiMo-H$_2$@NF, the relative intensities for Ni$^0$ and Mo$^{4+}$ signals decrease, accompanied by the appearance of Fe$^{3+}$ (BE = 711.8/725.1 eV) [32, 33] and increase of Ni$^{2+}$ signal as expected due to the cover of NiFe-LDH nanosheets on the NiMo-H$_2$ (Figs. 2(b)–2(d), and Table S3 in the ESM). Relative to NiMo-H$_2$@NF, NiFe-LDH@NiMo-H$_2$@NF shows a positive shift of BE for Ni$^0$ signal (from 852.5 to 852.7 eV) and Mo$^{4+}$ signal (from 229.4 to 229.7 eV). Meanwhile, relative to NiFe-LDH@NF, NiFe-LDH@NiMo-H$_2$@NF shows a negative shift of BE for Fe$^{3+}$ signal (from 712.2 to 711.8 eV) [33, 34]. The work functions ($W_f$) and charge density difference also indicate the electrons transfer from the NiMo-H$_2$ nanorods to the NiFe-LDH nanosheets (Fig. S5 in the ESM). The strong interaction between NiMo-H$_2$ and NiFe-LDH favors the reaction dynamics of water dissociation and the adsorption/desorption of intermediates, thus could boost the water electrolysis [33, 35, 36].

## 3.2 HER performance of NiFe-LDH@NiMo-H$_2$@NF

The HER electrocatalytic performances of NiFe-LDH@NiMo-H$_2$@NF, NiMo-H$_2$@NF, NiFe-LDH@NF, and commercial Pt/C

(20 wt.%) were examined in 1 M KOH aqueous electrolyte by a standard three-electrode system, as shown in Fig. 3. The NiFe-LDH@NF exhibits a high overpotential of 191 mV to deliver a current density of 10 mA·cm$^{-2}$, indicating the inert HER activities. The optimal NiMo-H$_2$@NF with reduction temperature of 450 °C presents a quite low overpotential of 46 mV at 10 mA·cm$^{-2}$ (Fig. 3(a), and Figs. S6 and S7 in the ESM). Surprisingly, by electrodepositing the NiFe-LDH nanosheets on the NiMo-H$_2$ nanorods, the NiFe-LDH@NiMo-H$_2$@NF presents a much lower overpotential of 26 mV at 10 mA·cm$^{-2}$, i.e., the HER-inert cover much improves the HER performance (Fig. S8 in the ESM). Even at the high current densities of 100 and 500 mA·cm$^{-2}$, the overpotentials are only 53 and 73 mV, respectively (Fig. 3(a)). Worthy to notice is that NiFe-LDH@NiMo-H$_2$@NF and Pt/C exhibit comparable HER performances in terms of overpotential (26 vs. 28 mV) at 10 mA·cm$^{-2}$ and Tafel plots (35.6 vs. 35.9 mV·dec$^{-1}$), while the former exhibits much lower overpotentials at high current densities of ≥100 mA·cm$^{-2}$ (Figs. 3(a)–3(c)). These results demonstrate that NiFe-LDH@NiMo-H$_2$@NF owns the best HER performance at all the current densities among the examined catalysts (Figs. 3(a) and 3(c), and Fig. S9 in the ESM), and outperforms most of Ni-, Mo-, Fe-based catalysts so far (Tables S1 and S2 in the ESM). The CP test indicates that NiFe-LDH@NiMo-H$_2$@NF also shows an extraordinary long-term durability in HER with a small overpotential increase of only 8 mV at an industrial-level current density of 500 mA·cm$^{-2}$ after 400 h (Fig. 3(d)), in agreement with the negligible change of the polarization curves (Fig. 3(e)). The Nyquist plots show that NiFe-LDH@NiMo-H$_2$@NF has the smallest charge transfer resistance ($R_{ct}$) of 0.79 Ω among all the catalysts, suggesting the best HER kinetics (Fig. S10 in the ESM).

As known, increasing pH value of electrolyte favors the water splitting reaction in the strong alkalinity [30, 37, 38]. Moreover, the HER performance of NiFe-LDH@NiMo-H$_2$@NF in 1 M KOH
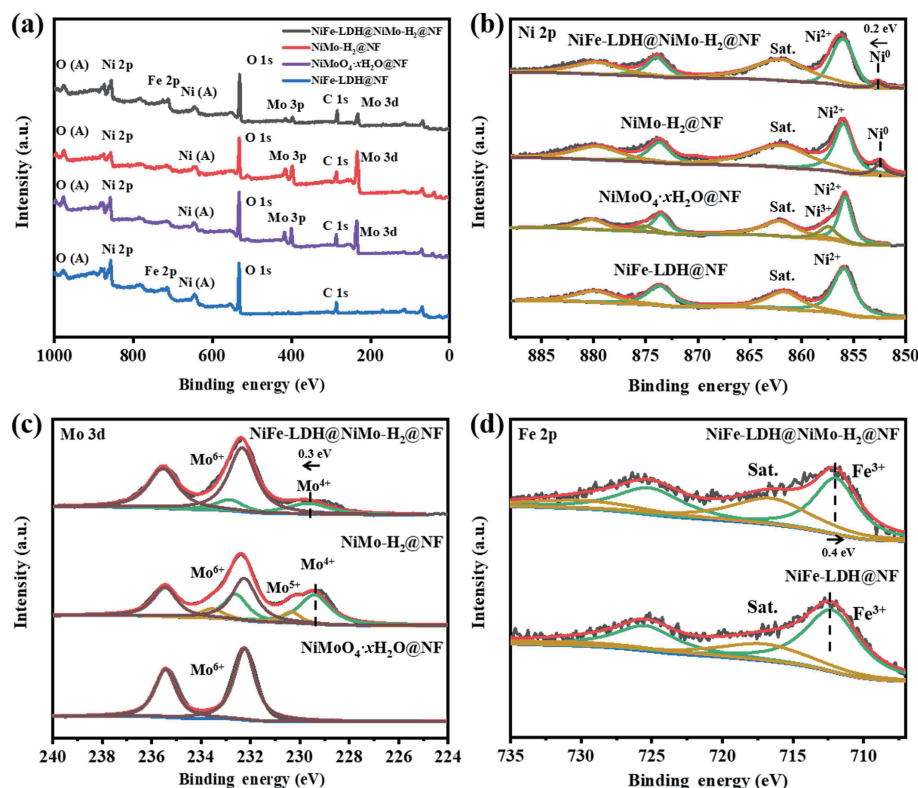


**Figure 2** XPS spectra for NiMoO$_4$·$x$H$_2$O@NF, NiMo-H$_2$@NF, and NiFe-LDH@NiMo-H$_2$@NF. (a) Survey spectra; (b) Ni 2p spectra; (c) Mo 3d spectra; (d) Fe 2p spectra. Notes: (1) Ni (A) and O (A) in (a) refer to corresponding element Auger peaks. (2) The XPS spectra for NiFe-LDH@NF in ((a), (b), and (d)) are presented for comparison. (3) In (b), the Ni$^0$ signal from nickel foam in NiMoO$_4$·$x$H$_2$O@NF can't be detected due to complete cover of NiMoO$_4$·$x$H$_2$O. The Ni$^0$ signals in NiMo-H$_2$@NF and NiFe-LDH@NiMo-H$_2$@NF come from NiMo-H$_2$.
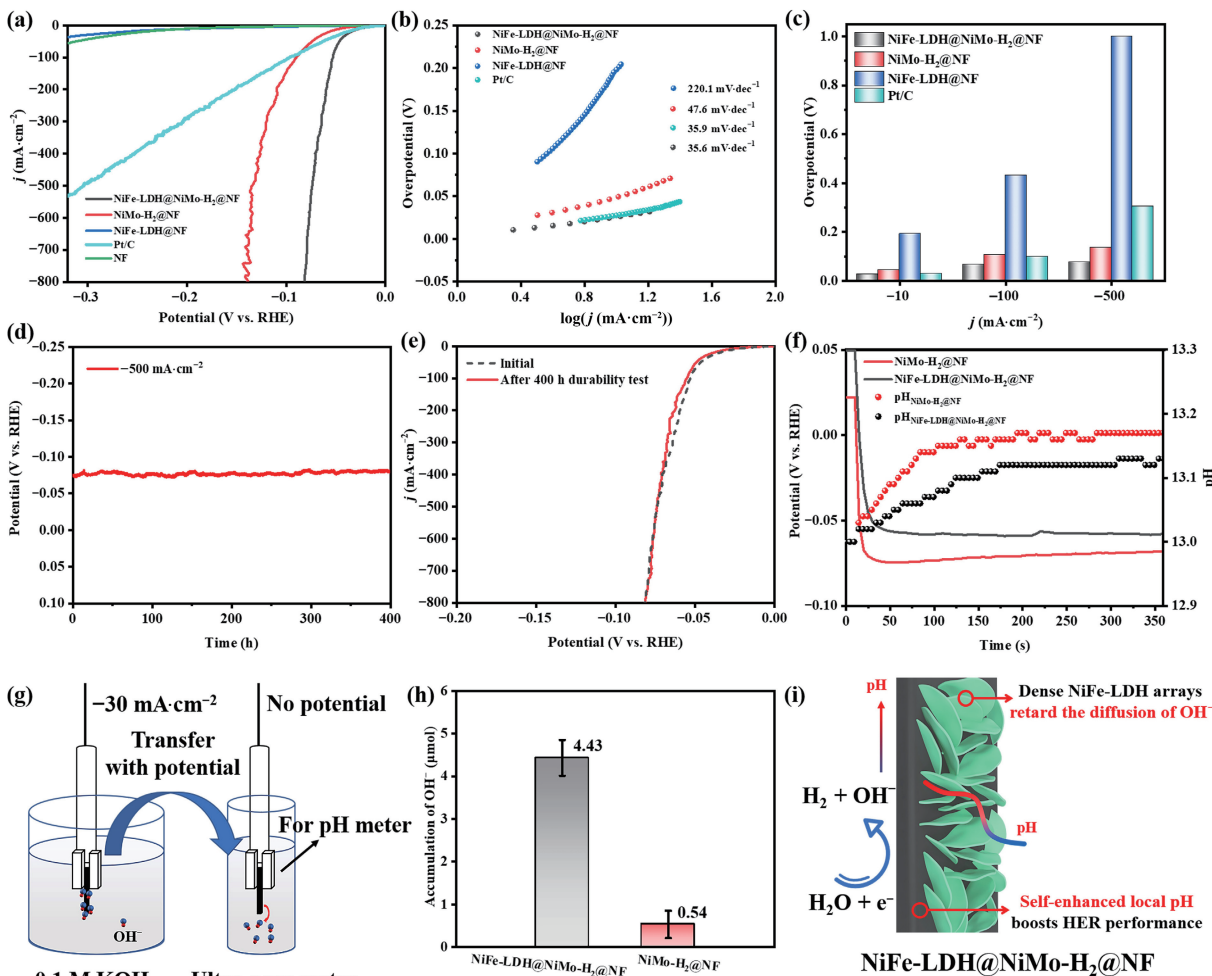
**Figure 3** HER performances of NiFe-LDH@NiMo-H$_2$@NF, NiMo-H$_2$@NF, NiFe-LDH@NF, and commercial Pt/C catalyst in 1 M KOH solution. (a) Polarization curves and (b) corresponding Tafel plots. (c) Overpotentials at the current densities of −10, −100, and −500 mA·cm$^{-2}$. (d) CP curve of NiFe-LDH@NiMo-H$_2$@NF at the current density of −500 mA·cm$^{-2}$ and (e) corresponding polarization curves before and after 400 h durability test. (f) CP curves and pH variations near the surface of catalysts of NiFe-LDH@NiMo-H$_2$@NF and NiMo-H$_2$@NF at −30 mA·cm$^{-2}$ in 0.1 M KOH solution. (g) Schematic diagram for measuring the OH$^-$ accumulations on catalysts and (h) the corresponding data on NiFe-LDH@NiMo-H$_2$@NF and NiMo-H$_2$@NF. (i) Illustration of structure–performance correlation in HER. Note: The curve of blank NF in (a) indicates its negligible contribution in all the catalysts.

is equivalent to that of NiMo-H$_2$@NF in 6 M KOH (Fig. S11 in the ESM). Hence, for NiFe-LDH@NiMo-H$_2$@NF, the boosting of the HER-inert NiFe-LDH cover to the HER performance of NiMo-H$_2$ nanorods can be attributed to the local pH increase at the HER active sites due to the retarded the diffusion of OH$^-$ ions generated during HER by the NiFe-LDH nanosheet arrays. To verify this point, the pH variations near the surface of NiFe-LDH@NiMo-H$_2$@NF and NiMo-H$_2$@NF are monitored during the CP test (Fig. S12 in the ESM). It is observed that more time is needed to achieve the stable pH with lower pH value for NiFe-LDH@NiMo-H$_2$@NF than NiMo-H$_2$@NF, i.e., 175 s@pH = 13.12 vs. 105 s@pH = 13.17 (Fig. 3(f)). With the same amount of OH$^-$ generated within the same time in CP test, this situation indicates the slower diffusion of OH$^-$ and higher local OH$^-$ concentration near active sites for the former, which leads to the lower overpotential for NiFe-LDH@NiMo-H$_2$@NF (57 mV@30 mA·cm$^{-2}$) than NiMo-H$_2$@NF (70 mV@30 mA·cm$^{-2}$) (Fig. 3(f)). The higher local OH$^-$ concentration is confirmed by directly measuring the OH$^-$ accumulations on catalysts. Specifically, after 10 min CP test, the working electrode was directly moved from the electrolyte to 5 mL ultra-pure water with the applied potential. After turning off the applied potential, the accumulated OH$^-$ on catalyst was released into the ultra-pure water and measured by pH meter (Fig. 3(g)). NiFe-LDH@NiMo-H$_2$@NF accumulated much more OH$^-$ than NiMo-H$_2$@NF (4.43 vs. 0.54 μmol) as expected (Fig. 3(h)). These

results demonstrate that the NiFe-LDH nanosheet arrays much increase the local pH near the HER-active sites of NiFe-LDH@NiMo-H$_2$@NF, leading to the much enhanced HER performance (Fig. 3(i)).

### 3.3 OER performance of NiFe-LDH@NiMo-H$_2$@NF

The OER electrocatalytic performances of NiFe-LDH@NiMo-H$_2$@NF, NiMo-H$_2$@NF, NiFe-LDH@NF, and commercial noble-metal catalysts are shown in Fig. 4. The NiFe-LDH@NiMo-H$_2$@NF shows an ultralow overpotential of 172 mV to deliver the current density of 10 mA·cm$^{-2}$, much lower than 277, 226, and 251 mV for NiMo-H$_2$@NF, NiFe-LDH@NF, and IrO$_2$, respectively (Fig. 4(a)). Low overpotentials of 218 and 239 mV are needed even for high current densities of 100 and 500 mA·cm$^{-2}$, respectively. The Tafel slope for NiFe-LDH@NiMo-H$_2$@NF is only 31.2 mV·dec$^{-1}$, much smaller than 70.2 mV·dec$^{-1}$ for NiMo-H$_2$@NF, 67.2 mV·dec$^{-1}$ for NiFe-LDH@NF, and 80.1 mV·dec$^{-1}$ for IrO$_2$, indicating the best OER kinetics (Fig. 4(b)). Generally, the NiFe-LDH@NiMo-H$_2$@NF exhibits the lowest overpotentials at all the current densities among the examined catalysts (Figs. 4(a) and 4(c), and Figs. S13 and S14 in the ESM), and locates at the top level of the Ni-, Mo-, Fe-based catalysts to date (Tables S1 and S2 in the ESM). The CP test shows an outstanding durability with only 11 mV increase in the overpotential at an industrial-level current density of 500 mA·cm$^{-2}$ after 400 h, in agreement with the
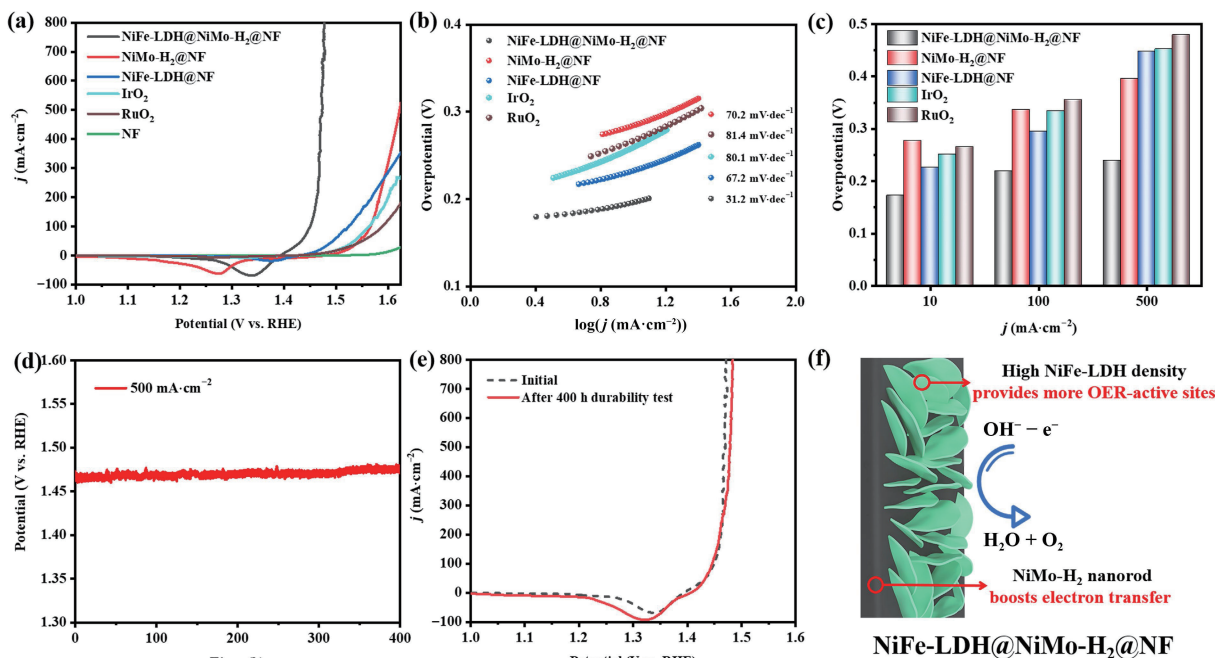
**Figure 4** OER performances of NiFe-LDH@NiMo-H$_2$@NF, NiMo-H$_2$@NF, NiFe-LDH@NF, and commercial noble-metal catalysts in 1 M KOH solution. (a) Polarization curves and (b) corresponding Tafel plots. (c) Overpotentials at the current densities of 10, 100, and 500 mA·cm$^{-2}$. (d) CP curve of NiFe-LDH@NiMo-H$_2$@NF at the current density of 500 mA·cm$^{-2}$ and (e) corresponding polarization curves before and after 400 h durability test. (f) Illustration of structure–performance correlation in OER. Note: The curve of blank NF in (a) is presented to indicate its negligible contribution in all the catalysts.

negligible change of the polarization curves (Figs. 4(d) and 4(e)).

The extraordinary OER performance of NiFe-LDH@NiMo-H$_2$@NF results from its large ECSA and small $R_{ct}$, as learnt from CV and EIS tests. The double-layer capacitance ($C_{dl}$, proportional to ECSA) and $R_{ct}$ of NiFe-LDH@NiMo-H$_2$@NF achieve 37.8 mF·cm$^{-2}$ and 0.38 Ω, respectively. The $C_{dl}$ (37.8 mF·cm$^{-2}$) is the largest and $R_{ct}$ (0.38 Ω) is the smallest ones among the examined catalysts in this study (Fig. S15 in the ESM).

The above results indicate that the hybridized 3D architecture of NiFe-LDH@NiMo-H$_2$@NF enables the high ECSA to provide more OER-active sites by increasing the NiFe-LDH nanosheet density (Figs. S13–S17 in the ESM), and also boosts the electron transfer due to the high conductivity of NiMo-H$_2$ nanorods, which synergistically improves the OER performance (Fig. 4(f)). In addition, the electrode fabricated by loading the slurry of NiMo-H$_2$ powder on NiFe-LDH@NF with Nafion binder exhibits much worse OER performance than the NiFe-LDH@NiMo-H$_2$@NF (Fig. S18 in the ESM), again indicating the promotion of the hybridized 3D architecture to OER.

### 3.4 OWS performance of NiFe-LDH@NiMo-H$_2$@NF

The OWS performances of NiFe-LDH@NiMo-H$_2$@NF, NiMo-H$_2$@NF, NiFe-LDH@NF, and commercial noble catalysts were evaluated in 1 M KOH solution, which shows much lower cell voltage of the electrolytic cell for NiFe-LDH@NiMo-H$_2$@NF than the others, as shown in Fig. 5. This nonprecious bifunctional catalyst only requires the low cell voltages of 1.45, 1.52, and 1.61 V to deliver the current densities of 10, 100, and 500 mA·cm$^{-2}$, respectively, much superior to the most reported bifunctional catalysts (Figs. 5(a)–5(c), and Tables S1 and S2 in the ESM). The CP test at the industrial-level current density of 500 mA·cm$^{-2}$ presents a negligible degradation (only 1.8%) of the cell voltage over 1000 h (Fig. 5(d) and Fig. S19 in the ESM). NiFe-LDH@NiMo-H$_2$@NF is almost unchanged after HER test as reflected by XRD and XPS characterizations, demonstrating its excellent durability for HER. In OER, the NiFeOOH species were *in situ* generated to act as active sites (Fig. S20 in the ESM). The catalysts at cathode and anode maintain the hybridized 3D

architecture without obvious changes (Fig. S21 in the ESM). All these results demonstrate the great potential of NiFe-LDH@NiMo-H$_2$@NF as an efficient, durable and cheap bifunctional catalyst for industrial water-splitting application.

## 4 Conclusions

In summary, we have successfully fabricated 3D-architectured NiFe-LDH@NiMo-H$_2$@NF bifunctional electrocatalysts by growing dense NiFe-LDH nanosheets on the conductive NiMo-based nanorods array deposited on Ni foam. As cathodic catalyst, the HER-inert NiFe-LDH nanosheet arrays retard the diffusion of OH$^-$ ions generated during HER, leading to a self-enhanced local pH on the HER-active sites of NiMo-H$_2$ and much boost HER performance thereof (26 mV@10 mA·cm$^{-2}$ and 74 mV@500 mA·cm$^{-2}$). As anodic catalyst, the dense NiFe-LDH nanosheet arrays provide the abundant OER-active sites and the highly conductive NiMo-H$_2$ nanorods effectively promote the electron transfer, leading to an outstanding OER performance (172 mV@10 mA·cm$^{-2}$ and 239 mV@500 mA·cm$^{-2}$). Benefitting by the excellent bifunctional catalytic performance of NiFe-LDH@NiMo-H$_2$@NF, the OWS cell demonstrates the extreme low voltages of 1.45 V@10 mA·cm$^{-2}$ and 1.61 V@500 mA·cm$^{-2}$, much lower than the commercial noble metal-based catalysts. In particular, at the industrial current density of 500 mA·cm$^{-2}$, the catalyst exhibits excellent long-term durability with little degradation (1.8%) of cell voltage for 1000 h, suggesting the great potential applications. This study provides an efficient strategy to develop advanced bifunctional electrocatalysts for OWS by rationally hybridizing HER- and OER-active components. For example, designing suitable 3D architectured catalysts to construct a local high pH environment could achieve high-performance OWS even in neutral medium.
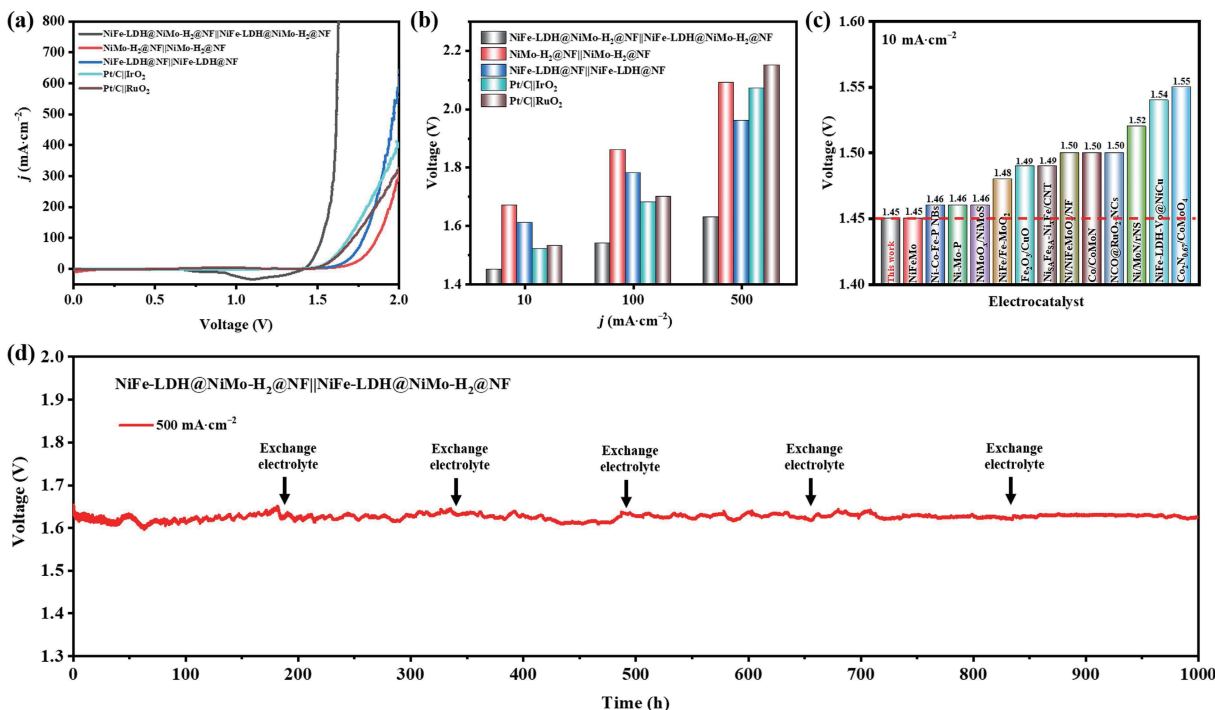
**Figure 5** Electrochemical performance of the overall water electrolytic cell. (a) Polarization curves. (b) Cell voltages at the current densities of 10, 100, and 500 mA·cm$^{-2}$. (c) Required cell voltage at a current density of 10 mA·cm$^{-2}$ for NiFe-LDH@NiMo-H$_2$@NF catalyst and other reported state-of-the-art bifunctional water splitting catalysts [39–51]. (d) Durability test of NiFe-LDH@NiMo-H$_2$@NF||NiFe-LDH@NiMo-H$_2$@NF at 500 mA·cm$^{-2}$.

**Electronic Supplementary Material:** Supplementary material (the detailed characterizations including SEM, TEM, STEM images, STEM-EDS spectrum, XPS and XRD spectra, additional electrochemical results, and the performance comparison with the literature) is available in the online version of this article at https://doi.org/10.1007/s12274-023-6303-9.

## References

[1] Yang, H. Y.; Driess, M.; Menezes, P. W. Self-supported electrocatalysts for practical water electrolysis. *Adv. Energy Mater.* **2021**, *11*, 2102074.

[2] Li, X.; Zhao, L. L.; Yu, J. Y.; Liu, X. Y.; Zhang, X. L.; Liu, H.; Zhou, W. J. Water splitting: From electrode to green energy system. *Nano-Micro Lett.* **2020**, *12*, 131.

[3] Hu, C. L.; Zhang, L.; Gong, J. L. Recent progress made in the mechanism comprehension and design of electrocatalysts for alkaline water splitting. *Energy Environ. Sci.* **2019**, *12*, 2620–2645.

[4] Xu, Q. C.; Zhang, J. H.; Zhang, H. X.; Zhang, L. Y.; Chen, L.; Hu, Y. J.; Jiang, H.; Li, C. Z. Atomic heterointerface engineering overcomes the activity limitation of electrocatalysts and promises highly-efficient alkaline water splitting. *Energy Environ. Sci.* **2021**, *14*, 5228–5259.

[5] Bai, S.; Wang, C. M.; Deng, M. S.; Gong, M.; Bai, Y.; Jiang, J.; Xiong, Y. J. Surface polarization matters: Enhancing the hydrogen-evolution reaction by shrinking Pt shells in Pt-Pd-graphene stack structures. *Angew. Chem., Int. Ed.* **2014**, *53*, 12120–12124.

[6] Seitz, L. C.; Dickens, C. F.; Nishio, K.; Hikita, Y.; Montoya, J.; Doyle, A.; Kirk, C.; Vojvodic, A.; Hwang, H. Y.; Norskov, J. K. et al. A highly active and stable IrO$_x$/SrIrO$_3$ catalyst for the oxygen evolution reaction. *Science* **2016**, *353*, 1011–1014.

[7] Chen, D.; Pu, Z. H.; Lu, R. H.; Ji, P. X.; Wang, P. Y.; Zhu, J. W.; Lin, C.; Li, H. W.; Zhou, X. G.; Hu, Z. Y. et al. Ultralow Ru loading transition metal phosphides as high‑efficient bifunctional

[8] electrocatalyst for a solar‑to‑hydrogen generation system. *Adv. Energy Mater.* **2020**, *10*, 2000814.

[8] Gao, F.; Zhang, Y. P.; Wu, Z. Y.; You, H. M.; Du, Y. K. Universal strategies to multi-dimensional noble-metal-based catalysts for electrocatalysis. *Coord. Chem. Rev.* **2021**, *436*, 213825.

[9] Liu, J. W.; Yang, X. Q.; Si, F. Z.; Zhao, B.; Xi, X. A.; Wang, L.; Zhang, J. J.; Fu, X. Z.; Luo, J. L. Interfacial component coupling effects towards precise heterostructure design for efficient electrocatalytic water splitting. *Nano Energy* **2022**, *103*, 107753.

[10] Peng, X.; Yan, Y. J.; Jin, X.; Huang, C.; Jin, W. H.; Gao, B.; Chu, P. K. Recent advance and prospectives of electrocatalysts based on transition metal selenides for efficient water splitting. *Nano Energy* **2020**, *78*, 105234.

[11] Zhao, Y.; Wei, S. Z.; Pan, K. M.; Dong, Z. L.; Zhang, B.; Wu, H. H.; Zhang, Q. B.; Lin, J. P.; Pang, H. Self-supporting transition metal chalcogenides on metal substrates for catalytic water splitting. *Chem. Eng. J.* **2021**, *421*, 129645.

[12] Yan, M. L.; Mao, K.; Cui, P. X.; Chen, C.; Zhao, J.; Wang, X. Z.; Yang, L. J.; Yang, H.; Wu, Q.; Hu, Z. *In situ* construction of porous hierarchical (Ni$_{3-x}$Fe$_x$)FeN/Ni heterojunctions toward efficient electrocatalytic oxygen evolution. *Nano Res.* **2020**, *13*, 328–334

[13] Yan, M. L.; Zhao, Z. Y.; Cui, P. X.; Mao, K.; Chen, C.; Wang, X. Z.; Wu, Q.; Yang, H.; Yang, L. J.; Hu, Z. Construction of hierarchical FeNi$_3$@(Fe,Ni)$_2$S$_2$ core–shell heterojunctions for advanced oxygen evolution. *Nano Res.* **2021**, *14*, 4220–4226.

[14] Xu, S. R.; Yu, X.; Luo, L.; Li, W. J.; Du, Y. S.; Kong, Q. Q.; Wu, Q. Multiscale manipulating induced flexible heterogeneous V-NiFe$_2$O$_4$@Ni$_2$P electrocatalyst for efficient and durable oxygen evolution reaction. *Nano Res.* **2022**, *15*, 4942–4949.

[15] Zhao, G. Q.; Rui, K.; Dou, S. X.; Sun, W. P. Heterostructures for electrochemical hydrogen evolution reaction: A review. *Adv. Funct. Mater.* **2018**, *28*, 1803291.

[16] Yu, M. Q.; Budiyanto, E.; Tüysüz, H. Principles of water electrolysis and recent progress in cobalt-, nickel-, and iron-based oxides for the oxygen evolution reaction. *Angew. Chem., Int. Ed.* **2022**, *61*, e202103824.

[17] Chandrasekaran, S.; Khandelwal, M.; Dayong, F.; Sui, L.; Chung, J. S.; Misra, R. D. K.; Yin, P.; Kim, E. J.; Kim, W.; Vanchiappan, A. et al. Developments and perspectives on robust nano‑and microstructured binder‑free electrodes for bifunctional water electrolysis and beyond. *Adv. Energy Mater.* **2022**, *12*, 2200409.

[18] Wu, Y. Y.; Li, G. D.; Liu, Y. P.; Yang, L.; Lian, X. R.; Asefa, T.; Zou, X. X. Overall water splitting catalyzed efficiently by an ultrathin nanosheet-built, hollow $Ni_3S_2$-based electrocatalyst. *Adv. Funct. Mater.* **2016**, *26*, 4839–4847.

[19] Li, W. J.; Deng, Y. Q.; Luo, L.; Du, Y. S.; Cheng, X. H.; Wu, Q. Nitrogen-doped $Fe_2O_3/NiTe_2$ as an excellent bifunctional electrocatalyst for overall water splitting. *J. Colloid Interface Sci.* **2023**, *639*, 416–423.

[20] Zhang, J.; Wang, T.; Liu, P.; Liao, Z. Q.; Liu, S. H.; Zhuang, X. D.; Chen, M. W.; Zschech, E.; Feng, X. L. Efficient hydrogen production on $MoNi_4$ electrocatalysts with fast water dissociation kinetics. *Nat. Commun.* **2017**, *8*, 15437.

[21] Ito, Y.; Ohto, T.; Hojo, D.; Wakisaka, M.; Nagata, Y.; Chen, L. H.; Hu, K. L.; Izumi, M.; Fujita, J. I.; Adschiri, T. Cooperation between holey graphene and NiMo alloy for hydrogen evolution in an acidic electrolyte. *ACS Catal.* **2018**, *8*, 3579–3586.

[22] Jiang, P.; Yang, Y.; Shi, R. H.; Xia, G. L.; Chen, J. T.; Su, J. W.; Chen, Q. W. Pt-like electrocatalytic behavior of $Ru-MoO_2$ nanocomposites for the hydrogen evolution reaction. *J. Mater. Chem. A* **2017**, *5*, 5475–5485.

[23] Zhou, D. J.; Li, P. S.; Lin, X.; McKinley, A.; Kuang, Y.; Liu, W.; Lin, W. F.; Sun, X. M.; Duan, X. Layered double hydroxide-based electrocatalysts for the oxygen evolution reaction: Identification and tailoring of active sites, and superaerophobic nanoarray electrode assembly. *Chem. Soc. Rev.* **2021**, *50*, 8790–8817.

[24] Zhai, P. L.; Wang, C.; Zhao, Y. Y.; Zhang, Y. X.; Gao, J. F.; Sun, L. C.; Hou, J. G. Regulating electronic states of nitride/hydroxide to accelerate kinetics for oxygen evolution at large current density. *Nat. Commun.* **2023**, *14*, 1873.

[25] Shin, H.; Xiao, H.; Goddard III, W. A. *In silico* discovery of new dopants for Fe-doped Ni oxyhydroxide ($Ni_{1-x}Fe_xOOH$) catalysts for oxygen evolution reaction. *J. Am. Chem. Soc.* **2018**, *140*, 6745–6748.

[26] Xiang, Q.; Wang, J.; Miao, Q.; Tao, P.; Song, C.; Shang, W.; Deng, T.; Yin, Z.; Wu, J. Recent progress in self-supported nanoarrays with diverse substrates for water splitting and beyond. *Mater. Today Nano* **2021**, *15*, 100120.

[27] Huang, C.; Chu, P. K. Recommended practices and benchmarking of foam electrodes in water splitting. *Trends Chem.* **2022**, *4*, 1065–1077.

[28] Yu, L.; Zhou, H. Q.; Sun, J. Y.; Qin, F.; Yu, F.; Bao, J. M.; Yu, Y.; Chen, S.; Ren, Z. F. Cu nanowires shelled with NiFe layered double hydroxide nanosheets as bifunctional electrocatalysts for overall water splitting. *Energy Environ. Sci.* **2017**, *10*, 1820–1827.

[29] Meng, X.; Li, Z. Q.; Liu, Y. Y.; Wang, Z. Y.; Wang, P.; Zheng, Z. K.; Dai, Y.; Huang, B. B.; Cheng, H. F.; He, J. H. Enabling unassisted solar water splitting with concurrent high efficiency and stability by robust earth-abundant bifunctional electrocatalysts. *Nano Energy* **2023**, *109*, 108296.

[30] Qian, G. F.; Chen, J. L.; Yu, T. Q.; Liu, J. C.; Luo, L.; Yin, S. B. Three-phase heterojunction NiMo-based nano-needle for water splitting at industrial alkaline condition. *Nano-Micro Lett.* **2021**, *14*, 20.

[31] Chen, Y. Y.; Zhang, Y.; Zhang, X.; Tang, T.; Luo, H.; Niu, S.; Dai, Z. H.; Wan, L. J.; Hu, J. S. Self-templated fabrication of $MoNi_4/MoO_{3-x}$ nanorod arrays with dual active components for highly efficient hydrogen evolution. *Adv. Mater.* **2017**, *29*, 1703311.

[32] Lv, J. J.; Wang, L. M.; Li, R. S.; Zhang, K. Y.; Zhao, D. F.; Li, Y. Q.; Li, X. J.; Huang, X. B.; Wang, G. Constructing a hetero-interface composed of oxygen vacancy-enriched $Co_3O_4$ and crystalline-amorphous NiFe-LDH for oxygen evolution reaction. *ACS Catal.* **2021**, *11*, 14338–14351.

[33] Wang, B. R.; Jiao, S. H.; Wang, Z. S.; Lu, M. J.; Chen, D.; Kang, Y. T.; Pang, G. S.; Feng, S. H. Rational design of NiFe LDH@$Ni_3N$ nano/microsheet arrays as a bifunctional electrocatalyst for overall water splitting. *J. Mater. Chem. A* **2020**, *8*, 17202–17211.

[34] Feng, X. T.; Jiao, Q. Z.; Chen, W. X.; Dang, Y. L.; Dai, Z.; Suib, S. L.; Zhang, J. T.; Zhao, Y.; Li, H. S.; Feng, C. H. Cactus-like $NiCo_2S_4$@NiFe LDH hollow spheres as an effective oxygen bifunctional electrocatalyst in alkaline solution. *Appl. Catal. B: Environ.* **2021**, *286*, 119869.

[35] Luo, M.; Yang, J. T.; Li, X. G.; Eguchi, M.; Yamauchi, Y.; Wang, Z. L. Insights into alloy/oxide or hydroxide interfaces in Ni-Mo-based electrocatalysts for hydrogen evolution under alkaline conditions. *Chem. Sci.* **2023**, *14*, 3400–3414.

[36] Lu, X. Y.; Cai, M. M.; Zou, Z. H.; Huang, J. F.; Xu, C. L. A novel MoNi@$Ni(OH)_2$ heterostructure with Pt-like and stable electrocatalytic activity for the hydrogen evolution reaction. *Chem. Commun.* **2020**, *56*, 1729–1732.

[37] Faid, A. Y.; Barnett, A. O.; Seland, F.; Sunde, S. Tuning $Ni-MoO_2$ catalyst-ionomer and electrolyte interaction for water electrolyzers with anion exchange membranes. *ACS Appl. Energy Mater.* **2021**, *4*, 3327–3340.

[38] Fan, K.; Xie, W. F.; Li, J. Z.; Sun, Y. N.; Xu, P. C.; Tang, Y.; Li, Z. H.; Shao, M. F. Active hydrogen boosts electrochemical nitrate reduction to ammonia. *Nat. Commun.* **2022**, *13*, 7958.

[39] Qin, F.; Zhao, Z. H.; Alam, M. K.; Ni, Y. Z.; Robles-Hernandez, F.; Yu, L.; Chen, S.; Ren, Z. F.; Wang, Z. M.; Bao, J. M. Trimetallic NiFeMo for overall electrochemical water splitting with a low cell voltage. *ACS Energy Lett.* **2018**, *3*, 546–554.

[40] Li, A.; Zhang, L.; Wang, F. Z.; Zhang, L.; Li, L.; Chen, H. M.; Wei, Z. D. Rational design of porous Ni-Co-Fe ternary metal phosphides nanobricks as bifunctional electrocatalysts for efficient overall water splitting. *Appl. Catal. B: Environ.* **2022**, *310*, 121353.

[41] Zhang, B.; Yang, F.; Liu, X. D.; Wu, N.; Che, S.; Li, Y. F. Phosphorus doped nickel-molybdenum aerogel for efficient overall water splitting. *Appl. Catal. B: Environ.* **2021**, *298*, 120494.

[42] Zhai, P. L.; Zhang, Y. X.; Wu, Y. Z.; Gao, J. F.; Zhang, B.; Cao, S. Y.; Zhang, Y. T.; Li, Z. W.; Sun, L. C.; Hou, J. G. Engineering active sites on hierarchical transition bimetal oxides/sulfides heterostructure array enabling robust overall water splitting. *Nat. Commun.* **2020**, *11*, 5462.

[43] Shi, W. J.; Zhu, J. W.; Gong, L.; Feng, D.; Ma, Q. L.; Yu, J.; Tang, H. L.; Zhao, Y. F.; Mu, S. C. Fe-incorporated $Ni/MoO_2$ hollow heterostructure nanorod arrays for high-efficiency overall water splitting in alkaline and seawater media. *Small* **2022**, *18*, 2205683.

[44] Hu, F.; Yu, D. S.; Ye, M.; Wang, H.; Hao, Y. N.; Wang, L. Q.; Li, L. L.; Han, X. P.; Peng, S. J. Lattice‐matching formed mesoporous transition metal oxide heterostructures advance water splitting by active Fe-O-Cu bridges. *Adv. Energy Mater.* **2022**, *12*, 2200067.

[45] Luo, W. H.; Wang, Y.; Luo, L. X.; Gong, S.; Wei, M. N.; Li, Y. X.; Gan, X. P.; Zhao, Y. Y.; Zhu, Z. H.; Li, Z. Single-atom and bimetallic nanoalloy supported on nanotubes as a bifunctional electrocatalyst for ultrahigh-current-density overall water splitting. *ACS Catal.* **2022**, *12*, 1167–1179.

[46] Li, Y. K.; Zhang, G.; Lu, W. T.; Cao, F. F. Amorphous Ni-Fe-Mo suboxides coupled with ni network as porous nanoplate array on nickel foam: A highly efficient and durable bifunctional electrode for overall water splitting. *Adv. Sci.* **2020**, *7*, 1902034.

[47] Ma, H. B.; Chen, Z. W.; Wang, Z. L.; Singh, C. V.; Jiang, Q. Interface engineering of Co/CoMoN/NF heterostructures for high-performance electrochemical overall water splitting. *Adv. Sci.* **2022**, *9*, 2105313.

[48] Zhang, Z. H.; Liu, X. H.; Wang, D.; Wan, H.; Zhang, Y.; Chen, G.; Zhang, N.; Ma, R. Z. Ruthenium composited $NiCo_2O_4$ spinel nanocones with oxygen vacancies as a high-efficient bifunctional catalyst for overall water splitting. *Chem. Eng. J.* **2022**, *446*, 137037.

[49] Chen, Y. K.; Wang, Y. J.; Yu, J. Y.; Xiong, G. W.; Niu, H. S.; Li, Y.; Sun, D. H.; Zhang, X. L.; Liu, H.; Zhou, W. J. Underfocus laser induced Ni nanoparticles embedded metallic MoN microrods as patterned electrode for efficient overall water splitting. *Adv. Sci.* **2022**, *9*, 2105869.

[50] Su, H.; Jiang, J.; Li, N.; Gao, Y. Q.; Ge, L. NiCu alloys anchored defect-rich NiFe layered double-hydroxides as efficient electrocatalysts for overall water splitting. *Chem. Eng. J.* **2022**, *446*, 137226.

[51] Hu, Y.; Luo, Z. Y.; Guo, M.; Dong, J. X.; Yan, P. X.; Hu, C.; Isimjan, T. T.; Yang, X. L. Interface engineering of $Co_2N_{0.67}/CoMoO_4$ heterostructure nanosheets as a highly active electrocatalyst for overall water splitting and $Zn-H_2O$ cell. *Chem. Eng. J.* **2022**, *435*, 134795.